https://doi.org/10.48048/tis.2024.7872

Innovative Waste Benzene Remediation by Enhanced Photocatalytic with TiO_2/Fe_3O_4-Based Material Supported by Bentonite in Batch and Continuous System

Emma Savitri, Stefanie Wiyono Yunita, Claudia Winoto and Restu Kartiko Widi*

Department of Chemical Engineering, Faculty of Engineering, University of Surabaya, Surabaya 60293, Indonesia

(*Corresponding author's e-mail: restu@staff.ubaya.ac.id)

Received: 21 December 2023, Revised: 18 January 2024, Accepted: 25 January 2024, Published: 10 May 2024

Abstract

Photocatalytic degradation of benzene is a viable and environmentally friendly method with significant economic advantages. In this study, a composite photocatalyst consisting of TiO_2 and Fe_3O_4 supported by bentonite was synthesized for benzene degradation. The objective was to assess the impact of critical parameters in both batch and continuous systems. The results showed that in batch system, the effects of initial benzene concentration and pH were explored, showing optimal degradation at an initial concentration of 400 ppm and pH 5. Under these conditions, an impressive % removal value of 95.334 % was achieved. Meanwhile, continuous system analysis showed a negative correlation between feed flow rate and % removal, with the most effective degradation occurring at a flow rate of 15 mL/min. The study also delivered into the kinetics of benzene degradation in batch system, obtaining a first-order reaction based on *Langmuir-Hinshelwood* model with a reaction rate constant (kr) of 85.68175 mg/(L.min) and an adsorption rate constant (K) of 0.0003002 L/mg. The adsorption model was observed to follow the Langmuir model. These results contributed to the optimization of photocatalytic benzene degradation processes, offering insights into the critical factors affecting efficiency in both batch and continuous systems. The established optimum conditions and kinetic parameters provided a foundation for future advancements in the design and application of composite photocatalysts for benzene remediation.

Keywords: Benzene, Composite, Photocatalytic, Adsorption, Degradation, Batch, Continuous

Introduction

Benzene, a ubiquitous and persistent environmental contaminant, is a recognized carcinogen, posing severe health risks to humans and ecosystems [1-3]. This substance is very dangerous and classified as VOC (Volatile Organic Compound). The widespread presence in air, water, and soil underscores the need for the development of efficient and sustainable removal strategies [4,5]. Conventional methods often need to provide a comprehensive solution due to the challenges associated with the stability and resistance of benzene to degradation [6].

In recent years, exploration of advanced materials and innovative technologies have been explored to overcome the challenges associated with benzene removal. Several methods to remove benzene in wastewater using physical, chemical, and biological methods include adsorption [7], oxidation [8,9], condensation [10], wet scrubbing [11], as well as membrane separation, and precipitation [12,13].

Photocatalysis has been proposed as a promising method for the degradation of benzene, leveraging the ability of photocatalysts to induce chemical transformations under light irradiation [14-16]. The ongoing progress in advanced oxidation processes, specifically photocatalytic oxidation (PCO), is crucial for addressing urgent challenges related to environmental pollution and potential risks to public health. The PCO technique has demonstrated efficacy in eradicating microorganisms and breaking down harmful chemical micropollutants in both water and air environments [17]. In this context, reactive oxygen species produced by wide-gap semiconductors offer an efficient means of decomposing pollutants through deep oxidation, representing a hopeful method for the degradation of VOC [18-20]. Several metal oxides have been studied and showed sufficiently good activity for the photodegradation of organic pollutants [21-27]. For example, titanium dioxide (TiO_2), with its well-documented photocatalytic properties was used for organic pollutants degradation [128-31]. However, to enhance the efficiency of photocatalytic processes, there is a growing interest in designing composite materials that combine multiple components synergistically.

Despite its advantages, TiO_2 faces a fundamental drawback related to the substantial width of its band gap. Specifically, for anatase TiO_2, the band gap measures 3.2 eV [32]. While TiO_2 can absorb UV radiation (< 390 nm), it fails to harness the majority (up to 95 %) of solar radiation corresponding to the visible region. This limitation has spurred the exploration of new photocatalysts that are active under visible light. In addition to other narrow-band semiconductors (e.g., Ag_3PO_4, $BiVO_4$) [33,34]. Recent advancements in the preparation of TiO_2 can potentially broaden its applications in photocatalytic processes. Modified TiO_2 with an extended action spectrum shows promise as a photocatalyst for efficiently degrading pollutants under visible light [35].

Integrating magnetic nanoparticles such as iron oxide (Fe_3O_4) in the composite also provides a magnetic response, enabling easy separation and recyclability of the catalyst from the treated medium. Fe_3O_4 plays a crucial role in controlling the size of TiO_2 anatase crystals [36,37], thereby addressing one of the challenges associated with the practical application of photocatalysts, and making the overall process more sustainable.

Bentonite, a clay mineral abundant in nature, offers a compelling choice as a component in such composites. The high surface area, porous structure, and cation exchange capacity make bentonite an excellent adsorbent for organic pollutants. Combining bentonite with photocatalysts such as TiO_2 can potentially improve the adsorption capacity of organic pollutants while concurrently facilitating photocatalytic degradation [38]. The synergy among bentonite, TiO_2, and Fe_3O_4 in a composite material has the potential to enhance benzene degradation through improved adsorption, efficient photocatalysis, and facile recovery of the catalyst.

Commonly, the degradation of benzene is conducted in both the gas phase or solution phases in a batch system [32]. Respectively, discovering a benzene photodegradation process implemented in a continuous system is rarely studied. This study was conducted to explore the synthesis, characterization, and application of such a composite, aiming to advance the understanding of its performance and mechanisms for the effective remediation of benzene-contaminated environments. The results are anticipated to contribute significantly to the field of environmental remediation and material science, offering a valuable step forward in the ongoing efforts to address benzene pollution.

This study aimed to explore the synthesis, characterization, and application of these composites by coating on ceramics for benzene photodegradation in continuous system. The results obtained are expected to increase understanding of performance for effective remediation of benzene-contaminated environments. Additionally, this study delved into the degradation reaction kinetics of benzene in the batch system.

Materials and methods

Materials

Materials used for the synthesis of TiO_2-Fe_3O_4-Bentonite photocatalyst materials were $TiCl_4$, $FeCl_2.4H_2O$, and $FeCl_3.6H_2O$. They were purchased from E. Merck. Natural bentonite was obtained from Pacitan, East Java, Indonesia. N_2 and O_2 gases was supplied by Samator, Indonesia.

Synthesis of photocatalyst material

The synthesis of bentonite-TiO_2-Fe_3O_4 photocatalyst material referred to a previous method [39,40]. The synthesis of TiO_2-Fe_3O_4-bentonite was conducted via the sol-gel method. The ratio molar of Ti: Fe was 1:3. The TiO_2 was synthesized by dissolving 2.75 mL of $TiCl_4$ in 50 mL of ethanol-water solution (1:1). The NH_4OH solution was added to the mixture until pH 7. The mixture was stirred continuously for 24 h to form a sol-gel phase. The Fe_3O_4 was synthesized by mixing 19.8 g of $FeCl_2.4H_2O$ and 27 g of $FeCl_3.6H_2O$ into 200 mL of 0.7 M NH_4OH solutions in the presence of N_2 gas. The Fe_3O_4 solid then was mixed with TMACl 2 % and NaOH solution until pH 12.1. The mixture was agitated for 24 h. After that, 140 mesh bentonite was dispersed in water for 24 h. Then, TiO_2, Fe_3O_4 and bentonite slurry were mixed and stirred at 50 °C for 24 h. After stirring, the mixture was washed with water to pH 7, dried and then calcined at a temperature of 500 °C for 6 h. Polyvinyl alcohol served as the binder for the photocatalyst material during ceramic coating. The application entailed coating a ceramic chamber with polyvinyl alcohol, allowing it to partially dry, then the photocatalyst was mixed with the binder at a ratio of 1:2 and applied to the ceramic surface using a spray method. Once the binder was completely dried, the ceramic chamber was considered ready for use in the degradation of benzene.

The examination of benzene concentration was carried out by Gas Chromatography (Agilent 7890A-GC). The column used was HP-PLOT Q size 30 m×0.53 mm×40 μm and the detector was Flame Ionization Detector (FID). The oven temperature was 150 °C for 2 min and then increased by 15 °C every minute until it reached 250 °C, also, the carrier gas used was helium.

Experimental setup for batch and continuous photocatalytic test

In the batch system, the experimental variables included initial benzene concentrations and solution pH, while the continuous system comprised varying feed flow rates. Benzene solution was introduced into a ceramic chamber coated with a photocatalyst and binder in batch setup. Subsequently, samples of 0.5 mL were extracted at specified intervals and analyzed using GC to determine benzene concentrations. The initial concentrations ranged from 100 to 500 ppm, and the pH values tested were 2, 5, and 10. The pH measurement was carried out using a pH meter, while adjustments were made with H_2SO_4 and NaOH solutions for acidic and basic conditions respectively. A processing system without UV light was also studied to compare the photocatalyst batch system. This system aims to observe the adsorption process that occurs in the system.

Meanwhile, in the continuous system, benzene solution at a specific concentration was continuously flowed through a ceramic chamber exposed to UV light, with varying flow rates. Once the chamber reached overflow after filling, 0.5 mL samples were collected at specific time intervals and analyzed using GC to quantify benzene concentrations. Feed flow rates were varied at 15, 25, 35, and 45 mL/min.

Results and discussion

Characterization

XRD analysis

In **Figure 1**, the characteristic peak of the TiO_2 anatase at $2\theta = 54{,}0274$, and magnetite phase (Fe_3O_4) at 30,3469, 35,8025, 43,4733, 57,4755, and 63,0634 are shown in XRD pattern. Anatase crystal was formed on the surface of bentonite more easily than the rutile phase [41-48]. The intensity of the magnetite phase surpassed that of TiO_2, primarily attributed to the predominant ratio of Fe_3O_4 in material preparation. The presence of magnetite plays a crucial role in regulating the formation of the TiO_2 anatase phase, thereby augmenting the photocatalyst process. Furthermore, the appearance of the peak associated with the TiO_2 anatase structure showed the crystalline formation within bentonite. This implies a relatively facile development of TiO_2 oxide on the surface of bentonite. The peak of bentonite phases was shown in the XRD pattern at $2\theta = 19{,}8572$ and 21,8051. The successful creation of the photocatalyst material was evidenced by the detection of three phases namely TiO_2 anatase, magnetite, and bentonite in the XRD analysis results. This achievement was attributed to the formation of TiO_2 in the anatase phase and Fe_3O_4 in the magnetite phase, both of which played significant roles in facilitating photocatalytic reactions.

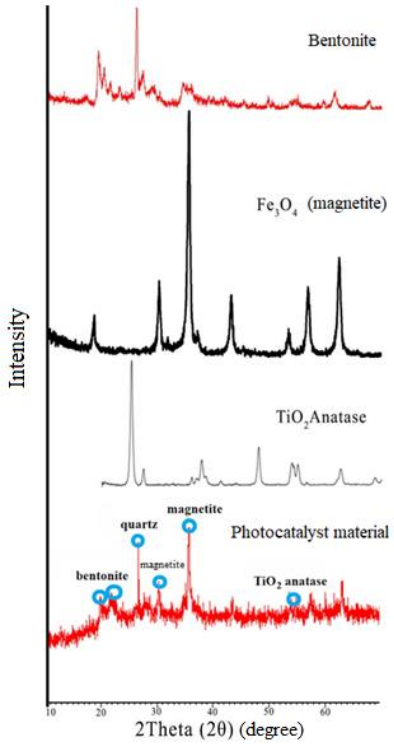

Figure 1 The XRD diffractogram of bentonite, Fe_3O_4, TiO_2 and photocatalyst material.

SEM-EDX analysis

The morphology of bentonite-TiO_2-Fe_3O_4 photocatalyst before (**Figure 2**) and after (**Figure 3**) use in the photodegradation of benzene was studied by microscope image. In **Figure 2**, the illustration showcases white particles, signifying the attachment of Ti and Fe to the ceramic tub through the use of a PVA (polyvinyl alcohol) binder. Following the benzene degradation process, the photocatalyst material remained affixed to the ceramic tub, as evident in **Figure 3**, where the obtained white particles showed the presence of Ti and Fe metals. Detailed quantitative information regarding the attachment of the photocatalyst material to the ceramic tub was presented in the EDX analysis results.

To quantify the reduction in each element, the EDX analysis results presented in **Table 1** were used, with the elements including O, C, Si, Fe, Al, Ti, Ca, Na, Mg, and K. The photocatalyst material primarily consisted of Ti, Fe, and O from TiO_2 and Fe_3O_4, while elements K, Na, Mg, and Al originated from the carrier within the photocatalyst material. The alterations in composition levels are detailed in **Table 1**, where the '-' signifies a reduction. The decrease in Ti and Fe levels after benzene degradation was attributed to the leaching of the photocatalyst material by the solution. This leaching resulted in reduced O levels in the EDX analysis, while an increase was observed in the levels of C, Si, Al, Ca, Na, Mg, and K.

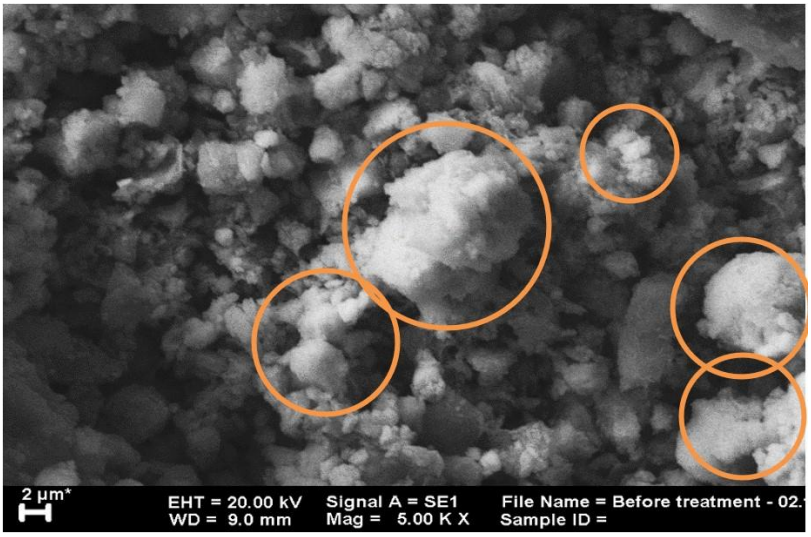

Figure 2 SEM image of photocatalyst material before used; (O) = metal oxides on pore of bentonite.

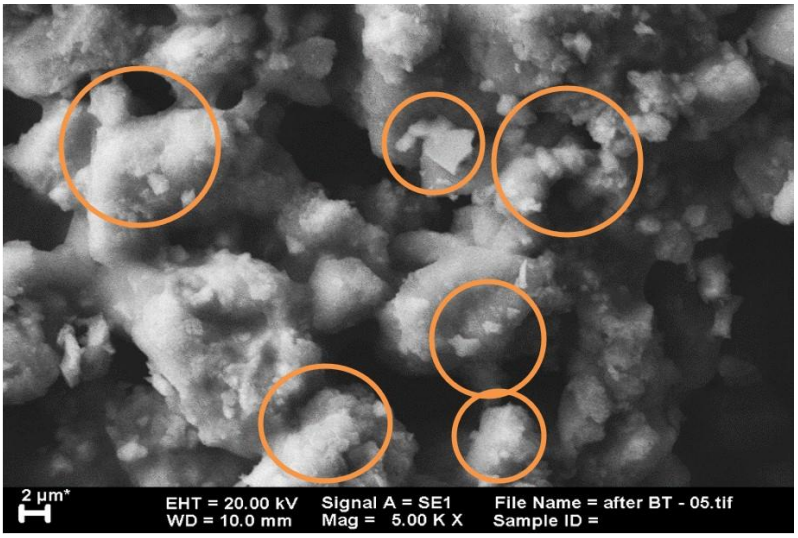

Figure 3 SEM image of photocatalyst material before used; (O) = metal oxides on pore of bentonite.

Table 1 Element percentage of EDX results before and after process (% w/w = percentage of weight/weight).

Elements	% w/w before used	% w/w after used	Δ
O	77.65	56.13	−21.52
C	7.82	23.65	15.38
Si	4.73	10.10	5.37
Fe	6.93	3.83	−3.1
Al	1.36	3.40	2.04
Ti	1.24	0.95	−0.29
Ca	0.12	0.67	0.55
Na	0	0.55	0.55
Mg	0.15	0.42	0.27
K	0	0.30	0.30

These data suggest 2 possible scenarios, firstly, it is plausible that only bentonite remains attached to the ceramic tub, while TiO_2 and Fe_3O_4 are carried away by benzene solution. This result was supported by the decreased levels of Ti and Fe as well as the increased amount of bentonite constituent. Secondly, it is possible that the entire photocatalyst material, including bentonite, is carried away by the benzene solution, resulting in elevated levels of C, Si, Al, Ca, Na, Mg, and K due to the ceramic composition. Based on the results, the leaching facilitated by the PVA binder was lower compared to the wall paint binders in a previous study [39,40].

Photodegradation of benzene in batch system

Effect of initial benzene concentration

In batch system, varying initial benzene concentrations were tested, ranging from 100 to 500 ppm. The % removal outcomes consistently exceeded 97 %, with the optimal % removal achieved at an initial concentration of 400 ppm, reaching 99.785 %. Beyond 400 ppm, the possibility of the photocatalyst material interacting with UV light decreased [49-53]. This decrease was attributed to the obstruction caused by benzene molecules, which impeded the formation of OH^*. The reduced reactivity of OH^* led to a decline in % removal. Additionally, at higher initial concentrations, competition for adsorption on the catalyst surface occurred due to the greater quantity of organic molecules in solution compared to the available active sites on the photocatalyst. This led to a decrease in % removal at concentrations exceeding 400 ppm. Conversely, lower concentrations resulted in suboptimal % removal due to the limited amount of benzene relative to water. The reduced availability of benzene hindered its contact and reaction with the photocatalyst material, leading to suboptimal % removal. Variations in initial benzene concentrations yielded almost identical % removal values, as the intervals between concentrations were narrow. **Figure 4** shows a decline in benzene concentration within the first 2 h, followed by a relatively constant concentration over the next 3 h. To facilitate the dissolution of benzene in water, ethanol was added, playing a crucial role in aiding the binding of benzene with water. This action promoted mutual dissolution, given the minimal solubility of benzene in water.

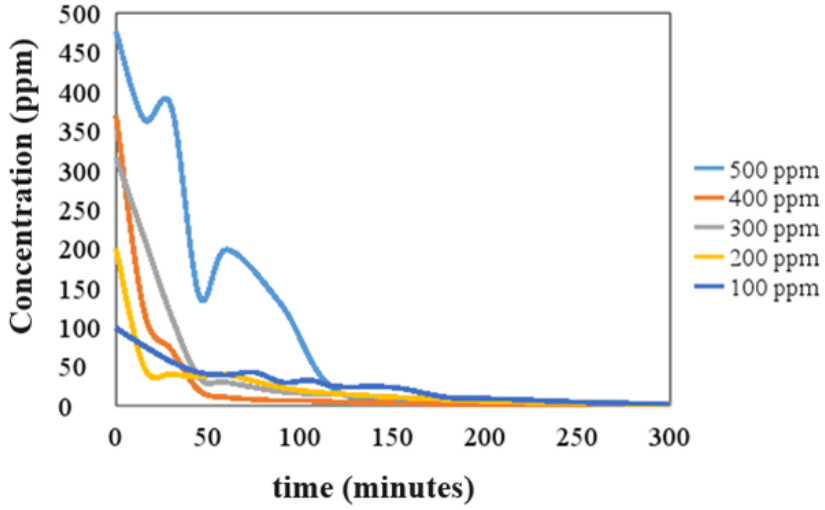

Figure 4 Decrease in benzene concentration with time in the photodegradation process at various initial benzene concentration.

Effect of pH

In the degradation of benzene solution through photocatalysis, the reaction comprised both adsorption and oxidation, with pH playing a crucial role in influencing these processes. According to Sharma *et al.* [54], the optimal pH for this reaction is 5. This optimal condition is based on the potential of zero charge (pHZPC) for the photocatalyst material and the isoelectric point (pHIEP) of benzene solution [39-40]. The potential of zero charge refers to the condition where the solid surface possesses a net charge of zero, while the isoelectric point represents the pH at which a macromolecule carries no net charge due to the addition or loss of protons through acid-base reactions. When the pH is below the isoelectric point of benzene solution, it becomes positively charged, but when the pH is above, it becomes neutral or negatively charged. Furthermore, the surface charge on the photocatalyst material significantly impacts benzene degradation. A competitive force arises in situations where the pH lies between the pHIEP of benzene solution and material. This attractive force makes benzene molecules readily adsorbed onto the photocatalyst material, thereby enhancing the degradation process. The pHIEP of benzene is reported as 4.45 [54], while the values for TiO_2 and Fe_3O_4 are 5.9 and 7.9, respectively. Bentonite, serving as the carrier, contains Ca^{2+}, Na^{+}, and Mg^{2+} ions, rendering it positively charged.

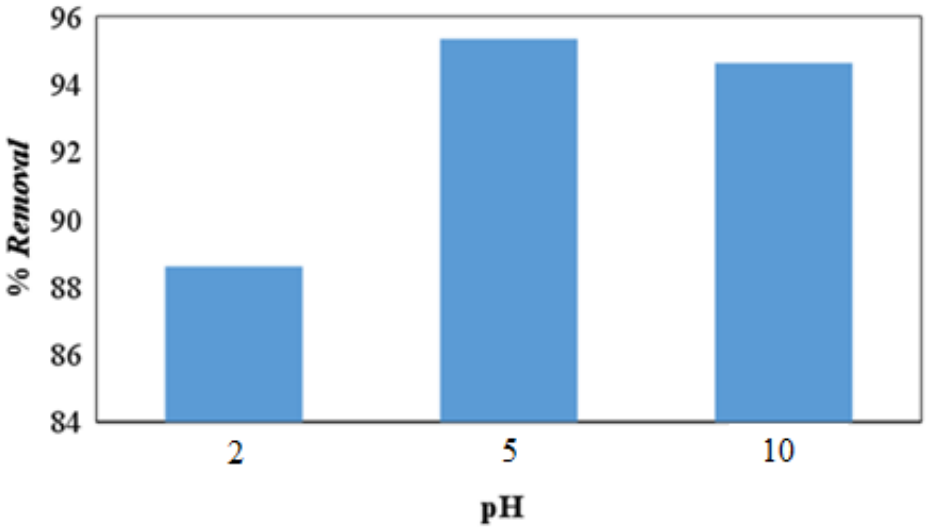

Figure 5 The effect of pH variation towards benzene percentage removal.

Figure 5 shows that % removal was lower under highly acidic and highly alkaline pH conditions compared to pH 5. In highly acidic conditions, the entire surface of the photocatalyst and benzene solution becomes positively charged, causing repulsion due to the lower pH than pHIEP and pHZPC. At pH 10, the entire surface of the catalyst and benzene solution became negatively charged, leading to repulsion because the pH was above the zero potential charge of the photocatalyst material and the isoelectric point of benzene solution. The optimal pH was obtained at pH 5, where benzene solution became negatively charged and the photocatalyst surface was positively charged, enhancing %removal. Based on the results, %removal values for each pH variation were 88.607, 95.334, and 94.622. At pH 10, %removal was higher than at pH 2 due to the final reaction forming CO_2 and H_2O, producing H_2CO_3. Carbonic acid, being a weak acid, had a significant impact on pH at 10, approaching the optimum conditions (pH 5) and resulting in higher % removal compared to acidic pH. **Table 2** shows a substantial decrease in pH from the initial conditions at 10, bringing the final pH closer to the optimal conditions at pH 5. This circumstance contributed to a significantly high % removal of benzene degradation under alkaline pH compared to acidic.

Table 2 Comparison of initial and final pH at various pH in benzene photodegradation.

Initial pH	Final pH
2.008	2.16
5.016	5.395
10.008	7.525

Kinetics of benzene photodegradation in batch system

Batch kinetics were computed using the initial concentration and the optimal pH, showing that within the initial 100 min, there was a reduction in benzene concentration, followed by a period of constancy. The determination of the reaction order in batch system was conducted using the formula proposed by Levenspiel [55]. The first-order kinetics was plotted with the equation $\ln \frac{C_{A0}}{C_A}$ against time, resulting in a linear regression of 0.9627 with a linear equation of y = 0.0198x, hence, the reaction rate constant was calculated as 0.0198/min. **Figure 6** shows that the experimental decline in benzene concentration over time was consistent with theoretical expectations.

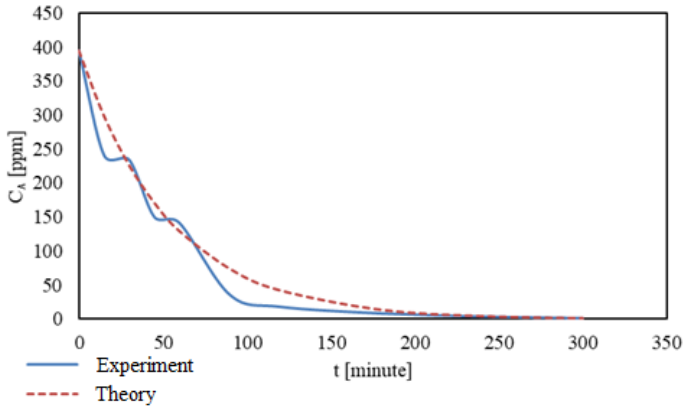

Figure 6 Assessment of the reduction in benzene concentration, examining the variance between experimental observations and theoretical predictions for first-order kinetics.

For the second-order kinetics, a plot was generated by plotting $\frac{1}{C_A}$ against time, resulting in a linear equation y = 0.0017x - 0.0736 with a linear regression of 0.793, yielding a reaction rate constant of 0.0017 L/(mg.min). The comparison of the experimental and theoretical decline in benzene concentration based on the second-order kinetics equation is depicted in **Figure 7**. Additionally, a t-test analysis was used to assess the precision between the two sets of data from the same population. For first-order kinetics, the t-test value was 90 %, while for second-order kinetics, the value was 21 %. The kinetics of benzene photocatalytic degradation reaction was consistent with first-order kinetics, signifying that the reaction rate was solely influenced by the concentration of benzene at a specific time and not by the concentration of OH^*.

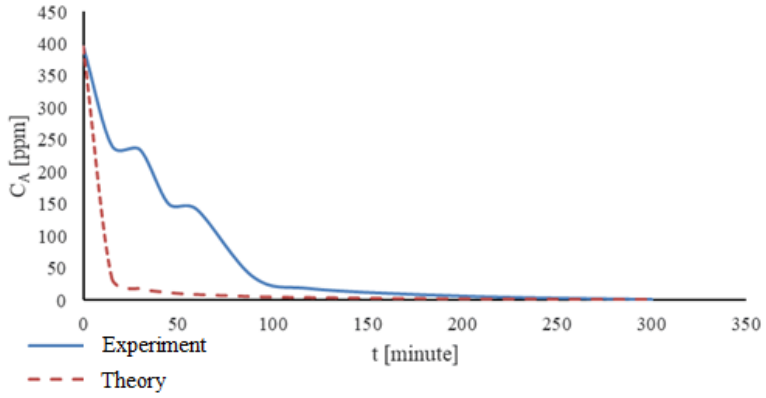

Figure 7 Assessment of the reduction in benzene concentration, examining the variance between experimental observations and theoretical predictions for second-order kinetics.

Langmuir-Hinshelwood

The kinetics of benzene degradation in photocatalytic reaction adhered to the Langmuir-Hinshelwood theory [56]. Experimental data were plotted with ln ($\frac{C_{Ao}}{C_A}$) on the y-axis and time on the x-axis, based on the equation ln ($\frac{C_{Ao}}{C_A}$) = K kr t - K (C_{Ao}-$C_{A)}$. In this equation, K represents adsorption rate constant, kr denotes the reaction rate constant, t is time, and C signifies the concentration of benzene. The plotted results yielded an R^2 value of 0.9599, with the linear equation being y = 0.0257x - 0.1131. According to the slope and intercept, the values of adsorption and reaction rate constants were K = 0.0003002 L/mg and kr = 85.68175 mg/(L.min) respectively. The higher value of kr compared to K showed the dominance of photocatalytic reaction over adsorption in the degradation process of benzene.

In batch system without UV lamps, the adsorption data were collected to determine equilibrium models, specifically the Freundlich and Langmuir. The Freundlich model is depicted by the formula $\log \frac{x}{m} = \frac{1}{n} \log C + \log K_F$, while the Langmuir model is represented by: $\frac{C}{\frac{x}{m}} = \frac{1}{K_L b} + \frac{1}{b} C$. It is stated in **Figures 8** and **9**.

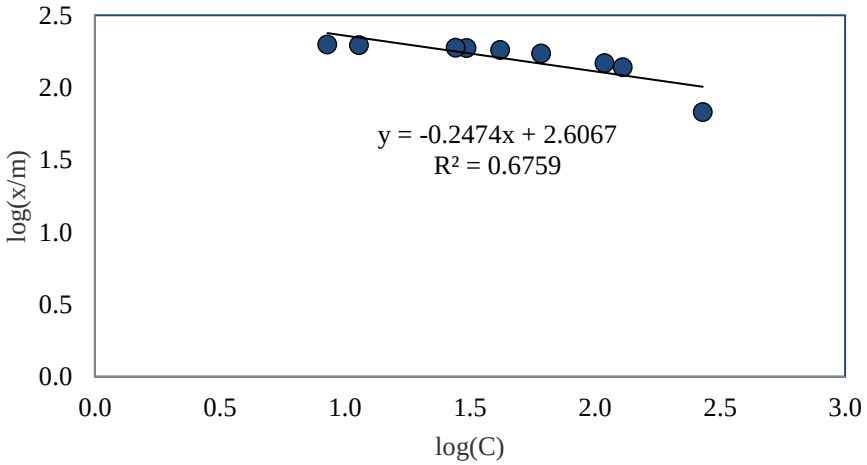

Figure 8 Langmuir adsorption isotherm model fitting with benzene adsorption on bentonite-TiO_2-Fe_3O_4.

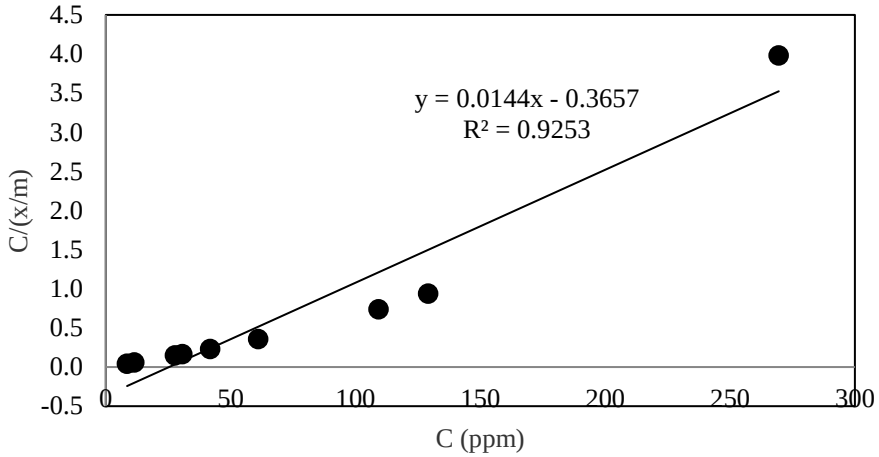

Figure 9 Freundlich adsorption isotherm model fitting with benzene adsorption on bentonite-TiO_2-Fe_3O_4.

The regression results from both models were compared, showing that the Langmuir model (r^2 = 0.9253) was closer to 1 than the Freundlich (r^2 = 0.6759). The obtained values for the Langmuir model constants were b (monolayer capacity) at 69.444 and the equilibrium constant at 0.0394. This adsorption model suggested the presence of active sites on the photocatalyst material surface, where the quantity was proportional to the surface area. Each active site selectively adsorbs one molecule through a physical or chemical bond [39-40]. Chemical interactions between bentonite and benzene in the molecular form can occur through ion exchange and chemical bonds. The negatively charged bentonite surface can interact with benzene, which has zero or slightly positive charge. It can produce electrostatic bonds between the bentonite and benzene surfaces. The silica surface can also have silanol groups (Si-OH), which can interact with benzene via hydrogen bonds. The experimental results indicated that the photocatalyst material showed homogenous adsorption capability and formed a monolayer.

Benzene degradation processes in continuous system

Effect of inlet flow rate

The impact of the inlet flow rate in Continuous System was influenced by the flow rate of benzene solution. The investigation aimed to determine the optimal % removal with variations in the inlet flow rate, specifically 15, 25, 35, and 45 mL/min. Based on the results, the % removal values observed were 76.836, 71.541, 60.684, and 52.547, respectively. This suggested that higher inlet flow rates led to lower % removal results. The critical factors influencing this outcome were the contact and residence time within the ceramic tub. For instance, at the same volume of the ceramic tub, an inlet flow rate of 15 mL/min resulted in a residence time of 97.28 min, while the inlet flow rate of 45 mL/min had a residence time of 32.427 min. The extended residence time at lower flow rates contributed to greater benzene degradation in the solution. The experimental results for various flow rate variations are detailed in **Table 3**.

Table 3 The efficiency at different variations of the inlet flow rate for an initial concentration of 400 ppm at pH 5.

Flow rate (mL/min)	τ (min)	% Removal
15	97.28	76.836
25	58.368	71.541
35	41.691	60.684
45	32.427	52.547

CSTR and PFR performance

In continuous system, there are 2 models, namely continuous stirred tank reactor (CSTR) and the plug flow reactor (PFR). The efficiency values for both CSTR and PFR were computed and compared experimentally. For the PFR model, the efficiency was calculated using the formula $X_A = 1 - e^{-k.\tau}$, while for the CSTR model, it was calculated with $X_A = \frac{1}{\frac{1}{k.\tau}+1}$ [55]. In these equations, k represents the reaction rate constant (per minute), X_A denotes the degradation of benzene conversion, and τ is the residence time (in minutes). The calculations presented in **Table 4** showed that the experimental results were more consistent with the performance of the PFR model compared to CSTR. This suggested that the absence of a mixing process in the ceramic tub during the degradation of benzene contributed to the experimental results being more consistent with the PFR performance. In the PFR model, the concentration of benzene changed at each point along the ceramic tub, from entry to exit. However, this study only analyzed the concentration exiting the ceramic tub.

Table 4 Comparative analysis of theoretical and experimental performance for CSTR and PFR models.

Flow rate (mL/min)	Trial (%)	CSTR (%)	ΔCSTR	PFR (%)	ΔPFR
15	76.83558	65.82533	11.01025	85.42910	8.59353
25	71.54140	53.61106	17.93034	68.51586	3.02554
35	60.68420	45.22020	15.46400	56.19798	4.48622
45	52.54709	39.10044	13.44665	47.37864	5.16845

Conclusions

In conclusion, this study underscores the viability of photocatalytic degradation as an environmentally friendly method for benzene remediation, accompanied by significant economic advantages. The synthesis of a TiO_2-Fe_3O_4-bentonite composite photocatalyst aimed to assess critical parameters in both batch and continuous systems. The research explored the effects of initial benzene concentration and pH in batch systems, while continuous system analysis focused on the correlation between feed flow rate and % removal. The initial concentration of benzene affects the efficiency of the degradation process in a batch system, where an increase in benzene concentration leads to an improvement in efficiency. However, excessive concentration results in a decrease in efficiency. From this study, an optimal initial concentration of 400 ppm was determined. pH influences the efficiency of the degradation process based on the isoelectric point of the photocatalytic material, and an optimum pH of 5 was obtained. The flow rate of benzene influences the efficiency of the degradation process in a continuous process, with higher flow rates leading to a decrease in efficiency. The optimal flow rate for the continuous system was found to be 15 mL/min.

Additionally, the study investigated the kinetics of benzene degradation in batch systems and analyzed the adsorption model. The reaction kinetics of the photocatalysis process follow first-order based on Langmuir-Hinshelwood kinetics, with a reaction rate constant (kr) of 85.68175 mg/(L.min) and an adsorption rate constant (K) of 0.0003002 L/mg. In a batch system without UV light, the adsorption process follows the Langmuir model, yielding a monolayer capacity constant of 69.444 mg/g and an equilibrium constant of 0.0394.

Overall, this research contributes valuable insights into the optimization of photocatalytic benzene degradation processes, offering a foundational understanding of critical factors affecting efficiency in both batch and continuous systems. The established conditions and parameters provide a basis for future advancements in the design and application of composite photocatalysts for benzene remediation, fostering progress in environmentally sustainable approaches to address benzene contamination.

Acknowledgements

We gratefully acknowledge financial support from Ministry of Research, Technology and Higher Education of the Republic of Indonesia (Hibah Penelitian Dasar Unggulan Perguruan Tinggi 2023) decree number 077/E5/PG.02.00.PL/2023 and contract number 004/SP2H/PT-L/LL7/2023 and 016/SP-Lit/LPPM-01/KemendikbudRistek/FT/V/2023.

References

[1] S Shajari, Eh Kowsari, N Seifvand, FB Ajdari, A Chinnappan, S Ramakrishna, G Saianand, MD Najafi, V Haddadi-Asl and S Abdpour. Efficient photocatalytic degradation of gaseous benzene and toluene over novel hybrid pil@tio2/m-go composites. *Catalysts* 2021; **11**, 126.

[2] K Li, Y He, J Li, J Sheng, Y Sun, J Li and F Dong. Identification of deactivation-resistant origin of $In(OH)_3$ for efficient and durable photodegradation of benzene, toluene and their mixtures. *J. Hazard. Mater.* 2021; **416**, 126208.

[3] W Qu, P Wang, M Gao, H Jun-Ya, Z Shen, Q Wang, R Li and D Zhang. Delocalization effect promoted the indoor air purification via directly unlocking the ring-opening pathway of toluene. *Environ. Sci. Tech.* 2020; **54**, 9693-701.

[4] C Dai, Y Zhou, H Peng, S Huang, P Qin, J Zhang, Y Yang, L Luo and X Zhang. Current progress in remediation of chlorinated volatile organic compounds: A review. *J. Ind. Eng. Chem.* 2018; **62**, 106-19.

[5] Q Wang, Y Li, A Serrano-Lotina, W Han, R Portela, R Wang, MA Bañares and KL Yeung. Operando investigation of toluene oxidation over 1D Pt@CeO_2 derived from Pt cluster-containing MOF. *J. Am. Chem. Soc.* 2021; **143**, 196-205.

[6] S Weon, F He and W Choi. Status and challenges in photocatalytic nanotechnology for cleaning air polluted with volatile organic compounds: Visible light utilization and catalyst deactivation. *Environ. Sci. Nano* 2019; **6**, 3185-214.

[7] S Yu, X Wang, H Pang, R Zhang, W Song, D Fu, T Hayat and X Wang. Boron nitride-based materials for the removal of pollutants from aqueous solutions: A review. *Chem. Eng. J.* 2018; **333**, 343-60.

[8] IC Sophiana, A Topandi, F Iskandar, H Devianto, N Nishiyama and YW Budhi. Catalytic oxidation of benzene at low temperature over novel combination of metal oxide based catalysts: CuO, MnO_2, NiO with $Ce_{0.75}Zr_{0.25}O_2$ as support. *Mater. Today Chem.* 2020; **17**, 100305.

[9] J Xie, X Li, J Guo, L Luo, JJ Delgado, N Martsinovich and J Tang. Highly selective oxidation of benzene to phenol with air at room temperature promoted by water. *Nat. Comm.* 2023; **14**, 4431.

[10] D Dubois, LT Iraci, EL Barth, F Salama, S Vinatier and E Sciamma-O'Brien. Investigating the condensation of benzene (C_6H_6) in titan's south polar cloud system with a combination of laboratory, observational, and modeling tools. *Planet. Sci. J.* 2021; **2**, 121.

[11] NF Idris, N Le-Minh, JE Hayes and RM Stuetz. Performance of wet scrubbers to remove VOCs from rubber emissions. *J. Environ. Manag.* 2022; **305**, 114426.

[12] J Zhou, G Yu, Q Li, M Wang and F Huang. Separation of benzene and cyclohexane by nonporous adaptive crystals of a hybrid[3]arene. *J. Am. Chem. Soc.* 2020; **142**, 2228-32.

[13] SH Rasheed, SS Ibrahim, QF Alsalhy and IK Salih. Separation of soluble benzene from an aqueous solution by pervaporation using a commercial polydimethylsiloxane membrane. *Membranes.* 2022; **12**, 1040.

[14] M Dubey, R Kumar, SK Srivastava and M Joshi. Visible light induced photodegradation of chlorinated organic pollutants using highly efficient magnetic Fe_3O_4/TiO_2 nanocomposite. *Optik* 2021; **243**, 167309.

[15] B Lei, W Cui, J Sheng, H Wang, P Chen, J Li, Y Sun and F Dong. Synergistic effects of crystal structure and oxygen vacancy on Bi_2O_3 polymorphs: Intermediates activation, photocatalytic reaction efficiency, and conversion pathway. *Sci. Bull.* 2020; **65**, 467-76.

[16] D Yuan, M Sun, S Tang, Y Zhang, Z Wang, J Qi, Y Rao and Q Zhang. All-solid-state $BiVO_4$/$ZnIn_2S_4$ Z-scheme composite with efficient charge separations for improved visible light photocatalytic organics degradation. *Chin. Chem. Lett.* 2020; **31**, 547-50.

[17] MM Rashid, B Simončič and B Tomšič. Recent advances in TiO_2-functionalized textile surfaces. *Surface. Interfac.* 2021; **22**, 100890.

[18] Z Rao, G Lu, A Mahmood, G Shi, X Xie and J Sun. Deactivation and activation mechanism of TiO_2 and rGO/Er^{3+}-TiO_2 during flowing gaseous VOCs photodegradation. *Appl. Catal. B Environ.* 2021; **284**, 119813.

[19] P Nagaraju, SH Puttaiah, K Wantala and B Shahmoradi. Preparation of modified ZnO nanoparticles for photocatalytic degradation of chlorobenzene. *Appl. Water Sci.* 2020; **10**, 137.

[20] P Chen, W Cui, H Wang, D Xing'an, J Li, Y Sun, Y Zhou, Y Zhang and F Dong. The importance of intermediates ring-opening in preventing photocatalyst deactivation during toluene decomposition. *Appl. Catal. B Environ.* 2020; **272**, 118977.

[21] F He, U Muliane, S Weon and W Choi. Substrate-specific mineralization and deactivation behaviors of TiO_2 as an air-cleaning photocatalyst. *Appl. Catal. B Environ.* 2020; **275**, 119145.

[22] D Rostamzadeh and S Sadeghi. Ni doped zinc oxide nanoparticles supported bentonite clay for photocatalytic degradation of anionic and cationic synthetic dyes in water treatment. *J. Photochem. Photobiol. Chem.* 2022; **431**, 113947.
[23] H Ghasemi, S Mozaffari, SH Mousavi, B Aghabarari and N Abu-Zahra. Decolorization of wastewater by heterogeneous Fenton reaction using MnO_2-Fe_3O_4/CuO hybrid catalysts. *J. Environ. Chem. Eng.* 2021; **9**, 105091.
[24] EC Nnadozie and PA Ajibade. Multifunctional magnetic oxide nanoparticle (MNP) core-shell: Review of synthesis, structural studies and application for wastewater treatment. *Molecules* 2020; **25**, 4110.
[25] R Ebrahimi, A Maleki, Y Zandsalimi, R Ghanbari, B Shahmoradi, R Rezaee, M Safari, SW Joo, H Daraei, SH Puttaiah and O Giahi. Photocatalytic degradation of organic dyes using WO_3-doped ZnO nanoparticles fixed on a glass surface in aqueous solution. *J. Ind. Eng. Chem.* 2019; **73**, 297-305.
[26] R Mahadevan, S Palanisamy and P Sakthivel. Role of nanoparticles as oxidation catalyst in the treatment of textile wastewater: Fundamentals and recent advances. *Sustain. Chem. Environ.* 2023; **4**, 100044.
[27] M Khatamian, B Divband and R Shahi. Ultrasound assisted co-precipitation synthesis of Fe_3O_4/ bentonite nanocomposite: Performance for nitrate, BOD and COD water treatment. *J. Water Process Eng.* 2019; **31**, 100870.
[28] SA Mamari, FE Suliman, Y Kim and R Selvaraj. Three-dimensional maple leaf CdS/g-C_3N_4 nanosheet composite for photodegradation of benzene in water. *Adv. Powder Tech.* 2023; **34**, 104026.
[29] I Ulhaq, W Ahmad, I Ahmad, M Yaseen and M Ilyas. Engineering TiO_2 supported CTAB modified bentonite for treatment of refinery wastewater through simultaneous photocatalytic oxidation and adsorption. *J. Water Process Eng.* 2021; **43**, 102239.
[30] C Santhosh, A Malathi, E Daneshvar, P Kollu and A Bhatnagar. Photocatalytic degradation of toxic aquatic pollutants by novel magnetic 3D-TiO_2@HPGA nanocomposite. *Sci. Rep.* 2018; **8**, 15531.
[31] M Ai, W Qin, T Xia, Y Ye, X Chen and P Zhang. Photocatalytic degradation of 2,4-dichlorophenol by TiO_2 intercalated talc nanocomposite. *Int. J. Photoenergy* 2019; **2019**, 1540271.
[32] X Liu, Y Zhang, S Matsushima, H Hojo and H Einaga. Photocatalytic oxidation process for treatment of gas phase benzene using Ti^{3+} self-doped TiO_2 microsphere with sea urchin-like structure. *Chem. Eng. J.* 2020; **402**, 126220.
[33] A Amirulsyafiee, MM Khan and MH Harunsani. Ag_3PO_4 and Ag_3PO_4-based visible light active photocatalysts: Recent progress, synthesis, and photocatalytic applications. *Catal. Comm.* 2022; **172**, 106556.
[34] M Gu, Y Yang, L Zhang, B Zhu, G Liang and J Yu. Efficient sacrificial-agent-free solar H_2O_2 production over all-inorganic S-scheme composites. *Appl. Catal. B Environ.* 2023; **324**, 122227.
[35] M Lyulyukin, N Kovalevskiy, A Bukhtiyarov, D Kozlov and D Selishchev. Kinetic aspects of benzene degradation over TiO_2-N and composite Fe/Bi_2WO_6/TiO_2-N photocatalysts under irradiation with visible light. *Int. J. Mol. Sci.* 2023; **24**, 5693.
[36] M Dubey, NV Challagulla, S Wadhwa and R Kumar. Ultrasound assisted synthesis of magnetic Fe_3O_4/α-MnO_2 nanocomposite for photodegradation of organic dye. *Colloid. Surface. Physicochem. Eng. Aspect.* 2021; **609**, 125720.
[37] Z Dong, Q Zhang, BY Chen and J Hong. Oxidation of bisphenol A by persulfate via Fe_3O_4-α-MnO_2 nanoflower-like catalyst: Mechanism and efficiency. *Chem. Eng. J.* 2019; **357**, 337-47.
[38] RK Widi. Pillared interlayered clays (PILCs): Harnessing their potential as adsorbents and catalysts - a mini review. *In*: Proceedings of the 4th International Conference on Informatics, Technology and Engineering 2023, Jogyakarta, Indonesia. 2023, p. 439-53
[39] RK Widi, E Savitri, A Budhyantoro, R Yasaputera and J Gunardi. Application of photocatalyst material bentonite ti based as antimicrobial paint. *Int. J. Adv. Sci. Eng. Inform. Tech.* 2020; **10**, 2498.
[40] RK Widi, I Suciani, E Savitri, R Reynaldi and A Budhyantoro. Photocatalytic decolorization of basic blue 41 using TiO_2 -Fe_3O_4-bentonite coating applied to ceramic in continuous system. *Chem. Eng. Comm.* 2020; **207**, 203-12.
[41] NS Allen, N Mahdjoub, V Vishnyakov, PJ Kelly and RJ Kriek. The effect of crystalline phase (anatase, brookite and rutile) and size on the photocatalytic activity of calcined polymorphic titanium dioxide (TiO_2). *Polymer Degrad. Stabil.* 2018; **150**, 31-6.
[42] G Nagaraj, D Brundha, C Chandraleka, M Arulpriya, V Kowsalya, S Sangavi, R Jayalakshmi, S Tamilarasu and R Murugan. Facile synthesis of improved anatase TiO_2 nanoparticles for enhanced solar-light driven photocatalyst. *SN Appl. Sci.* 2020; **2**, 734.
[43] YJO Asencios, VS Lourenço and WA Carvalho. Removal of phenol in seawater by heterogeneous

photocatalysis using activated carbon materials modified with TiO_2. *Catal. Today* 2020; **388**-**389**, 247-58.

[44] Y Cardona, A Węgrzyn, P Miśkowiec, SA Korili and A Gil. Catalytic photodegradation of organic compounds using TiO_2/pillared clays synthesized using a nonconventional aluminum source. *Chem. Eng. J.* 2022; **446**, 136908.

[45] MS Cergel and F Atay. The role of the annealing process in different gas environments on the degradation of the methylene blue organic pollutant by brookite-TiO_2 photocatalyst. *Ionics* 2019; **25**, 3823-36.

[46] X Yu, J Xie, Q Liu, H Dong and Y Li. The origin of enhanced photocatalytic activity in g-C_3N_4/TiO_2 heterostructure revealed by DFT calculations. *J. Colloid Interface Sci.* 2021; **593**, 133-41.

[47] VR Akshay, B Arun, G Mandal and M Vasundhara. Structural, optical and magnetic behavior of sol-gel derived Ni-doped dilute magnetic semiconductor TiO_2 nanocrystals for advanced functional applications. *Phys. Chem. Chem. Phys.* 2019; **21**, 2519-32.

[48] L Velardi, L Scrimieri, A Serra, D Manno and L Calcagnile. Effect of temperature on the physical, optical and photocatalytic properties of TiO_2 nanoparticles. *SN Appl. Sci.* 2020; **2**, 707.

[49] Z Wang, P Feng, H Chen and Q Yu. Photocatalytic performance and dispersion stability of nanodispersed TiO_2 hydrosol in electrolyte solutions with different cations. *J. Environ. Sci.* 2020; **88**, 59-71.

[50] DB Miklos, C Remy, M Jekel, KG Linden, JE Drewes and U Hübner. Evaluation of advanced oxidation processes for water and wastewater treatment - A critical review. *Water Res.* 2018; **139**, 118-31.

[51] HB Hadjltaief, ME Galvez, MB Zina and PD Costa. TiO_2/clay as a heterogeneous catalyst in photocatalytic/photochemical oxidation of anionic reactive blue 19. *Arabian J. Chem.* 2019; **12**, 1454-62.

[52] I Mironyuk, L Soltys, T Tatarchuk and V Tsinurchyn. Ways to improve the efficiency of TiO_2-based photocatalysts: Review. *Phys. Chem. Solid State* 2020; **21**, 300-11.

[53] SAH Deba, BA Wols, DR Yntema and RGH Lammertink. Photocatalytic ceramic membrane: Effect of the illumination intensity and distribution. *J. Photochem. Photobiol. Chem.* 2023; **437**, 114469.

[54] A Sharma and BK Lee. Growth of TiO_2 nano-wall on activated carbon fibers for enhancing the photocatalytic oxidation of benzene in aqueous phase. *Catal. Today* 2017; **287**, 113-21.

[55] PR Gunjal and VV Ranade. Chapter 7 - Catalytic reaction engineering. *Ind. Catalytic Process. Fine Specialty Chem.* 2016; **2016**, 263-314.

[56] M Dubey, U Bhan and R Kumar. Chapter 6 - Catalytic remediation of chlorinated organic compounds (COCs) in wastewater. *Emerg. Trends Approaching Zero Waste* 2022; **2022**, 133-51.